



HAL
open science

In Situ Electron Paramagnetic Resonance Correlated Spectroscopy and Imaging: A Tool for Lithium-Ion Batteries to Investigate Metallic Lithium Sub-Micrometric Structures Created by Plating and Stripping

Charles Emmanuel Dutoit, Mingxue Tang, Gourier Didier, Jean-marie Tarascon, Hervé Vezin, Elodie Salager

► **To cite this version:**

Charles Emmanuel Dutoit, Mingxue Tang, Gourier Didier, Jean-marie Tarascon, Hervé Vezin, et al.. In Situ Electron Paramagnetic Resonance Correlated Spectroscopy and Imaging: A Tool for Lithium-Ion Batteries to Investigate Metallic Lithium Sub-Micrometric Structures Created by Plating and Stripping. 2020. hal-03000546

HAL Id: hal-03000546

<https://hal.science/hal-03000546>

Preprint submitted on 12 Nov 2020

HAL is a multi-disciplinary open access archive for the deposit and dissemination of scientific research documents, whether they are published or not. The documents may come from teaching and research institutions in France or abroad, or from public or private research centers.

L'archive ouverte pluridisciplinaire **HAL**, est destinée au dépôt et à la diffusion de documents scientifiques de niveau recherche, publiés ou non, émanant des établissements d'enseignement et de recherche français ou étrangers, des laboratoires publics ou privés.

***In situ* electron paramagnetic resonance correlated spectroscopy and imaging: a tool for lithium-ion batteries to investigate metallic lithium sub-micrometric structures created by plating and stripping**

Charles-Emmanuel Dutoit^{1,2,*†}, Mingxue Tang^{1,2‡}, Didier Gourier³, Jean-Marie Tarascon^{2,4}, Hervé Vezin^{5,*} & Elodie Salager^{1,2}

¹CNRS, CEMHTI UPR3079, Université d'Orléans, 45071 Orléans, France

²Réseau sur le Stockage Electrochimique de l'Energie (RS2E), FR CNRS 3459, France

³Chimie-ParisTech, PSL Université, CNRS, Institut de Recherche de Chimie-Paris (IRCP), 75005 Paris, France

⁴Collège de France, CNRS FRE3357, 75005 Paris, France

⁵Université Lille Nord de France, CNRS UMR8516, LASIR, 59655 Villeneuve d'Ascq, France

1 **Monitoring the formation of dendrites or filaments of lithium is of paramount importance**
2 **for Li-based battery technologies, hence the intense activities in designing *in situ* techniques**
3 **to visualize their growth. Herein we report the benefit of correlating *in situ* electron para-**
4 **magnetic resonance (EPR) spectroscopy and EPR imaging to analyze the morphology and**
5 **location of metallic lithium in a symmetric Li/LiPF₆/Li electrochemical cell during polariza-**
6 **tion. We exploit the variations in shape, resonance field and amplitude of the EPR spectra**
7 **to follow, *operando*, the nucleation of sub-micrometric Li particles (narrow and symmetrical**

[†]Present address: Chimie-ParisTech, PSL Université, CNRS, Institut de Recherche de Chimie-Paris (IRCP), Paris, France

[‡]Present address: Center for high pressure science and technology advanced research, Beijing, China

8 signal) that conjointly occurs with the fragmentation of bulk Li on the opposite electrode
9 (asymmetrical signal). Moreover, *in situ* EPR correlated spectroscopy and imaging (spectral-
10 spatial EPR imaging) allows the identification (spectral) and localization (spatial) of the sub-
11 micrometric Li particles created by plating (deposition) or stripping (altered bulk Li surface).
12 We finally demonstrate the possibility to visualize, via *in situ* EPR imaging, dendrites formed
13 through the separator in the whole cell. Such a technique could be of great help in mastering
14 the Li-electrolyte interface issues that plague the development of solid-state batteries.

15 Introduction

16 Rechargeable lithium-ion batteries (LIBs) are recognized for the good balance between weight,
17 volume and electrochemical performance. Despite the wide range of applications for LIBs, pre-
18 vention of non-uniform deposition of metallic lithium is still of paramount importance to avoid in-
19 ternal short-circuits and thermal runaway. Formation of lithium dendrites on the negative graphitic
20 electrode is an issue in mature LIBs that prevents faster charge, essential for the development
21 of transport electrification,^{1,2} while lithium filament growth hinders the spread of all-solid-state
22 batteries.^{3,4}

23 Metallic lithium deposition in batteries is still relatively hard to predict, and the visualization,
24 in real time, of its location, morphology and growth is the subject of intense development for many
25 techniques.⁵ A precious feature of Electron Paramagnetic Resonance (EPR) is the combination
26 of imaging and spectroscopy, unexplored to date for the characterization of lithium deposition in
27 batteries. In 2015 *in situ* EPR was demonstrated as a tool of choice to detect Li deposits, either

28 by imaging⁶ or spectroscopy.⁷ In continuation of the latter an extensive study by *operando* EPR
29 spectroscopy was performed for Li plating on graphite.⁸ Niemöller et al. also studied, *ex situ*, the
30 potential and limitations of *ex situ* EPR imaging (EPRI) on metallic Li⁹.

31 In this paper, we report the combination of *in situ* X-band EPR spectroscopy and imaging
32 to observe directly, *in situ*, the morphology and the distribution of metallic lithium in a symmetric
33 Li/LiPF₆/Li electrochemical cell. We observe the roughening of the lithium surface upon strip-
34 ping, the spatially inhomogeneous electrodeposition of the sub-micrometric lithium particles and
35 dendrite growth causing a short-circuit.

36 **Results and discussion**

37 Figure 1a shows a schematic representation of the Li/LiPF₆/Li electrochemical cell placed in the
38 EPR resonator, with the static magnetic field \mathbf{H} oriented along the \mathbf{Z} axis and the microwave field
39 along the \mathbf{Y} axis. The magnetic field gradients, used for imaging, are oriented along the \mathbf{Y} and
40 \mathbf{Z} axes. This configuration is optimized to study lithium exchange between the two electrodes
41 and especially dendritic growth. The EPR spectrum of the assembled electrochemical cell in the
42 pristine state, before applying the current flow, is shown in fig. 1c. It is identical to the spectrum
43 of a metallic lithium disk (fig. 1b), as expected. The resonance field and therefore the measured g
44 factor ($g=2.0030$, close to the free electron spin $g=2.0023$) is characteristic of metallic lithium.

45 Previous EPR investigations showed that the lineshape, linewidth and intensity were highly
46 dependent on the morphology of metallic lithium.^{6,7,9} The EPR spectrum lineshape of a metallic

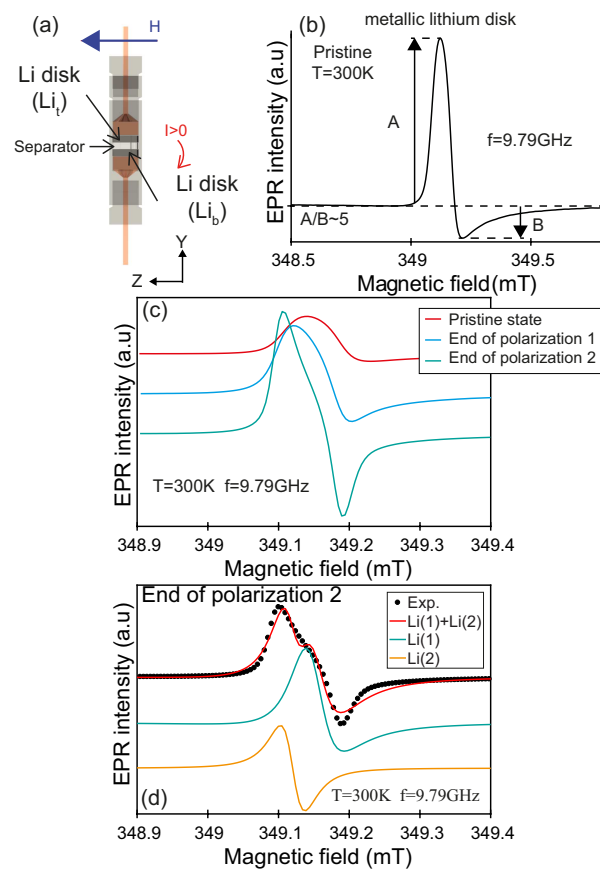


Figure 1: (Colour online) *Operando* EPR spectroscopy recorded at 9.79 GHz. (a) Schematic representation of the EPR electrochemical cell and its orientation in the external magnetic field \mathbf{H} . \mathbf{Y} and \mathbf{Z} are the magnetic field gradient directions for imaging. (b) cw-EPR spectrum of a pristine metallic lithium disk (no cycling). A and B denote the amplitude of the positive and negative parts of the EPR line respectively. (c) Selection of *operando* cw-EPR spectra of the Li/LiPF₆/Li cell. A symmetrical and sharp EPR line appears in the low magnetic field flank of the bulk signal upon polarization. (d) Experimental (black dots) and simulated (red line) EPR spectra at the end of polarization 2. The dysonian component of the simulation Li(1) is assigned to the bulk Li signal of both electrodes and the lorentzian component Li(2) to the newly formed sub-micrometric Li particles.

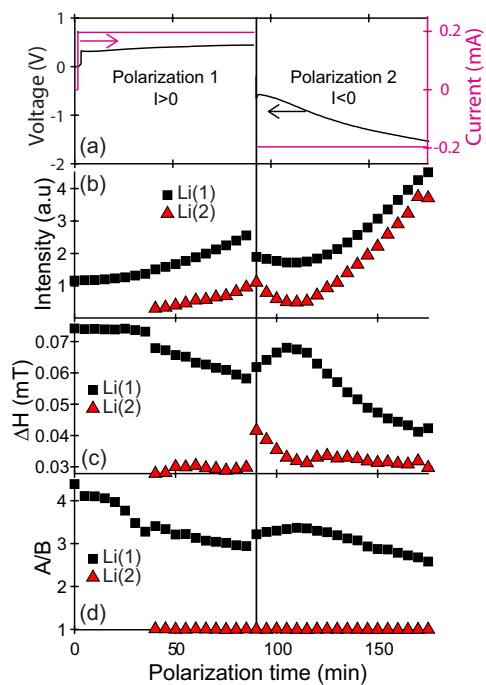


Figure 2: (Colour online) Evolution of the cw-EPR parameters versus polarization time for the two components, Li(1) (bulk Li) and Li(2) (micrometric particles). (a) Voltage (left) and current (right) of the electrochemical cell, (b) EPR spectrum intensity, (c) linewidth ΔH and (d) asymmetry ratio A/B.

47 conductor is indeed controlled by the limited penetration depth δ_{mw} of the microwave field in the
48 metal, known as the skin effect: ¹⁰

$$\delta_{mw} \propto \sqrt{\frac{\rho}{f}} \quad (1)$$

49 ρ being the metal resistivity and f the microwave frequency.

50 More precisely the EPR spectrum lineshape depends on the metal thickness d compared
51 to δ_{mw} . If $d > \delta_{mw}$, only the spins located inside the skin depth are excited by the microwave
52 field. During the spin coherence time T_2 , each electron travels on a distance of the order of
53 $\delta_{eff} \approx (D_e T_2)^{\frac{1}{2}}$ where D_e is the diffusion coefficient of electrons.^{10,11} As $\delta_{eff} \approx 60 \mu m$ in metal-
54 lic lithium,⁹ the electrons penetrate several times in the skin region during T_2 ($\sim 10^{-9}$ sec), and
55 thus experience each time a microwave pulse, resulting in an asymmetrical (dysonian) lineshape
56 classically characterized by the asymmetry ratio $A/B \approx 5$.^{10,11} If $d < \delta_{mw}$, all the electronic spins
57 experience the same microwave field, resulting in a symmetrical Lorentzian EPR line. Conse-
58 quently the presence of sub-micrometric metallic lithium such as dendritic and/or mossy structures
59 can be revealed by the shape of the EPR spectrum. As expected for a Li electrode in the pristine
60 state (fig.1b), a single dysonian lineshape with $A/B \approx 5$ is observed, typical of thick metal. This is
61 in good agreement with the thickness $d=400 \mu m$ of the Li electrode, which is much larger than the
62 skin depth $\delta_{mw} \approx 1 \mu m$ for Li at 9.6 GHz.^{6,7}

63 The Li//Li cell was polarized to follow the mechanisms of Li stripping and plating with a

64 current density of 1 mA/cm^2 (fig. 2a). During polarization 1, the top Li electrode is oxidized (Li
65 stripping) and the bottom electrode is reduced (Li electroplating). In polarization 2 this process is
66 reversed. No sign of cell failure was observed after 175 min of positive and negative polarization.
67 Three spectra of the cell, corresponding to the pristine state ($t=0 \text{ min}$), the end of polarization
68 1 ($t=85 \text{ min}$) and the end of polarization 2 ($t=175 \text{ min}$), are shown in fig.1c. Between the two
69 polarization steps, the cell was left in open circuit (OCV) to record *in situ* EPR images. In contrast,
70 EPR spectra were recorded *operando* during the polarization steps, that is with current flowing
71 through the cell. The spectra exhibit different lineshapes, indicative of a modification of the Li
72 electrode morphologies upon polarization. The growth of a narrow and symmetric line in the
73 low field flank of the bulk Li signal results in a splitting of the EPR spectrum (fig. 1c). Each
74 EPR spectrum was simulated by the sum of two contributions: (i) a dysonian line for bulk Li
75 (Li(1)) with an asymmetry ratio $4 > A/B > 2$, a fixed resonance field $H_{res}=349.15 \text{ mT}$ and a varying
76 linewidth ΔH ; (ii) a narrow ($\Delta H \sim 0.03\text{-}0.4 \text{ mT}$) and symmetric ($A/B \sim 1$) lorentzian line (Li(2))
77 with resonance field $H_{res}=349.12 \text{ mT}$ (corresponding to $g=2.0032$), lower than for bulk lithium.
78 This new EPR line is assigned to Li particles with size $d < 1 \mu\text{m}$, as discussed above. An example
79 of simulation is given in fig. 1d. The evolution of the EPR spectrum parameters for the two Li
80 species (intensity, linewidth ΔH and asymmetry A/B) during cell operation are given in fig. 2. The
81 intensities of the simulated lines continuously increase as the cell is polarized, to reach a factor 4
82 at the end of polarization 2 ($t=175 \text{ min}$), as shown in fig. 2b. This increase in the EPR intensity
83 is assigned to the growth of sub-micrometric Li particles (Li(2)) on both electrodes but also to the
84 increased intensity of the EPR line of bulk Li (Li(1)). The latter should not be misinterpreted as

85 an increase in the total quantity of metallic Li during polarization. This increased intensity of bulk
86 Li signal (Li(1)) is the direct consequence of the progressive decrease of the asymmetry ratio A/B
87 from 5 to less than 3 at the end of polarization 2 (fig. 2d). This feature is the manifestation of the
88 alteration of the two bulk electrode surfaces during cycling, which creates Li structures with size
89 approaching the skin depth δ_{mw} . As only electron spins in the volume of the skin are responsible
90 for the EPR signal, the roughening of bulk lithium at constant total volume of metal induces an
91 increase of the skin volume, and thus an increase of the EPR intensity. The decrease of ΔH (fig.
92 2c) for bulk lithium during polarization is also the consequence of the progressive decrease of A/B
93 for the bulk Li signal.

94 This evolution of the EPR signal during cell cycling indicates that the reaction $\text{Li}^0 \rightarrow \text{Li}^+$
95 $+ e^-$ (1) at one electrode and the reverse reaction $\text{Li}^+ + e^- \rightarrow \text{Li}^0$ (2) at the other electrode are
96 not equivalent. In polarization 1, newly formed sub-micrometric Li particles are produced on the
97 bottom electrode (Li_b) with reaction (2), while the progressive roughening of the bulk Li electrode
98 on top (Li_t) occurs through reaction (1). It seems, however, that there is a beginning of reversible
99 behaviour in the first few minutes of polarization 2, when the current is reversed, with a decrease
100 in EPR intensity of both types of lithium, as well an increase of the A/B ratio and the linewidth
101 ΔH of bulk lithium (fig. 2). This could indicate that the previously-formed Li microparticles
102 on Li_b are partially consumed by reaction (1) and/or structures of lithium in electrode Li_t are
103 fused together into larger structures through reaction (2). In the second part of polarization 2,
104 however, the general evolution observed during polarization 1 continues, with an increase in the
105 EPR intensities of both Li types, and a decrease of A/B and ΔH of bulk lithium (fig. 2). This

106 demonstrates the high sensitivity of *in situ* EPR spectroscopy to the nucleation of very small Li
107 particles and the roughening of bulk Li electrodes, and places it as a tool of choice for studying the
108 effect of prolonged cycling.

109 Interestingly, the resonance field H_{res} of EPR line for the sub-micrometric Li particles is
110 shifted to low field by 0.03 mT compared to the bulk Li signal. Although the nature of this shift
111 requires further studies, it is likely that it is produced by the dynamic nuclear polarization of
112 metallic lithium particles via the Overhauser effect: ¹²⁻¹⁴ the partial saturation of the EPR line po-
113 larizes the nuclear spins, which create a very small nuclear field H_{nuc} of around 0.03 mT, adding
114 to the external field H_0 . As the spins resonate in the effective field $H_{eff}=H_0+H_{nuc}>H_0$, the res-
115 onance condition, $hf=g\mu_B(H_{res}+H_{nuc})$ requires that H_{res} decreases when H_{nuc} increases. This
116 effect is maximum when the electron spins "experience" all the nuclear spins, as in the case of
117 the sub-micrometric Li particles. A recent NMR investigation showed that Dynamic Nuclear Po-
118 larization (DNP) of metallic lithium was a powerful technique for characterizing electrodeposited
119 microstructures.¹⁵

120 In summary, the surface of the stripped Li electrode roughens during electrochemical po-
121 larization, with structures of micrometric size or slightly larger, and new Li particles of sub-
122 micrometric size nucleate through electroplating on the opposite electrode. In order to visualize
123 and locate these two types of metallic Li in the electrochemical cell, we performed *in situ* electron
124 paramagnetic resonance imaging (EPRI) of the full cell (fig. 3a, b, c). EPR images were recorded
125 in the pristine state, at the end of polarization 1 and of polarization 2, in open-circuit phases to

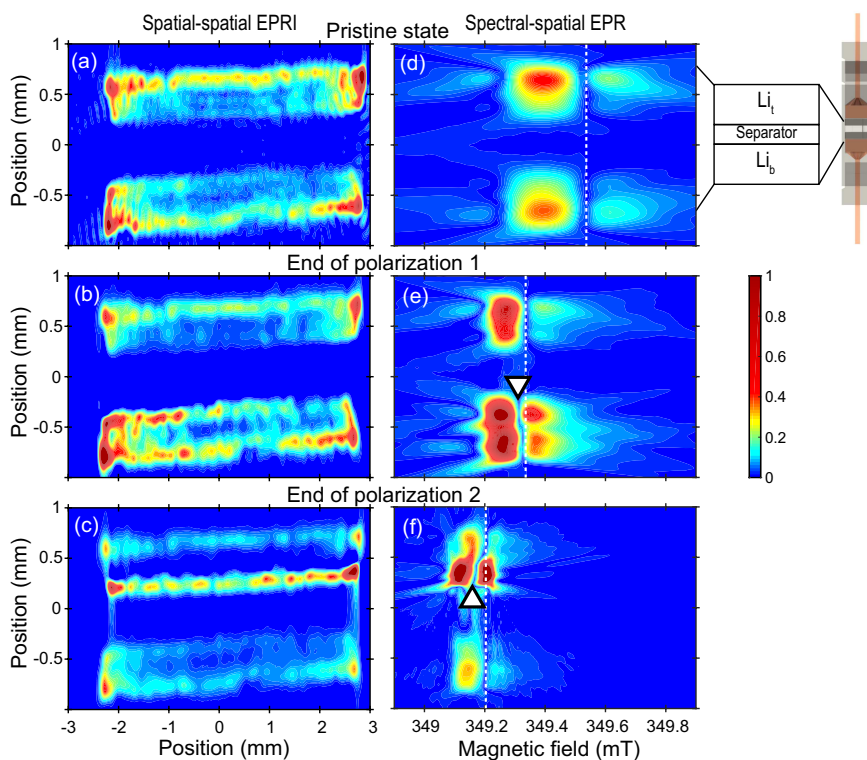


Figure 3: (Colour online) *In situ* X-band EPR spatial-spatial images (left) and spectral-spatial images (right) of the cell in the pristine state (top), at the end of polarization 1 (middle) and at the end of polarization 2 (bottom). The images display the absolute value of the EPR line $|d\chi''/dH|$. The vertical dashed line indicates the resonance field of the bulk Li signal and the white triangle the resonance field of the sharper component (guides to the eye). The field of the vertical dashed line shifts between spectral-spatial EPR images due to a change of the microwave frequency. The color bar indicates the color code for the intensities, identical for all plots.

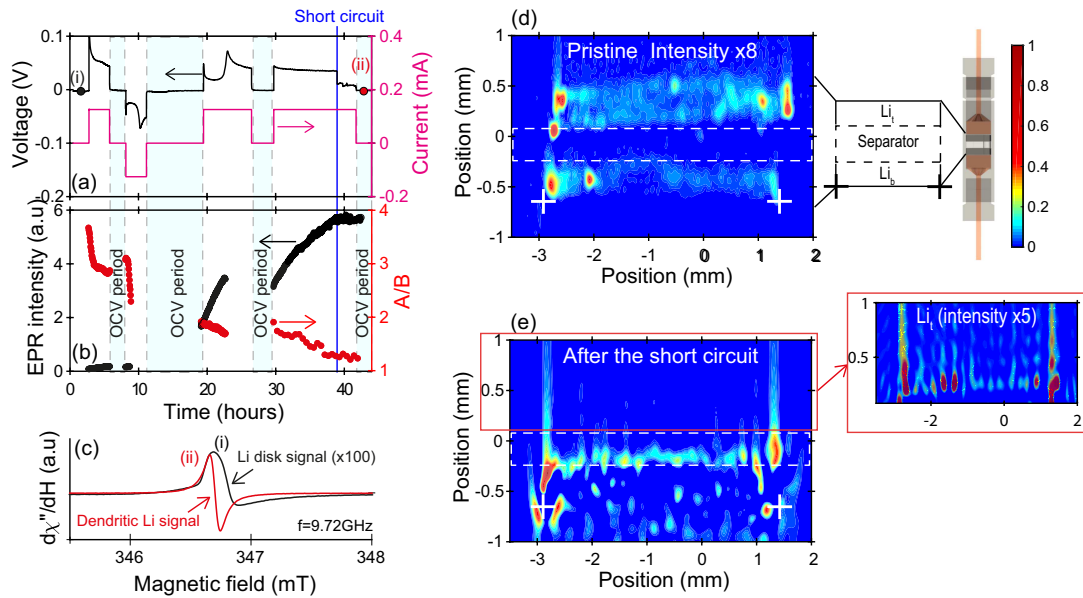


Figure 4: (Colour online) *In situ* detection (EPR spectrum) and localization (EPR 2D images) of dendritic Li . (a) Voltage and current of the electrochemical cell versus time. The vertical blue line indicates the short circuit with a voltage drop to 0 V and current still flowing in the cell. (b) *Operando* intensity and A/B ratio measured on the entire EPR signal (no simulation) as a function of time. (c) EPR spectra of the cell recorded in the pristine state (bulk Li electrodes) and after the short circuit (dendritic Li). The resonance field is $H_{res}=346.82$ mT for the bulk Li signal and $H_{res}=346.7$ mT for the dendritic Li signal. (d, e) *In situ* spatial-spatial EPR images recorded in the pristine state (intensity x8) and after the short circuit, respectively. Spots crossing the separator after the short circuit suggest the location of dendritic Li. The inset shows a zoom in the region of the top electrode Li_t , not fully consumed. The white crosses are a guide to the eye for the lower part of the bottom electrode.

126 prevent compositional evolution during recording. First, pure two-dimensional imaging (spatial-
127 spatial mode) was tested, with a gradient of 175 G/cm for encoding spatially the lithium signal.
128 Thanks to the sharp EPR lines of metallic Li (<1 G) the EPR images can be obtained with a high
129 spatial resolution of the order of micrometers in the pristine state.^{9,16}

130 Spatial-spatial EPR images are shown in fig. 3(left). They confirm that metallic Li is located
131 only in the two electrodes initially (fig. 3a). The separator inside the cell, with a thickness of
132 500 μm , appears in the center from the absence of EPR signal during all the electrochemical steps.
133 Its apparent size is similar to the real size and is indicative of a relatively good alignment of the
134 cell. In principle, one would expect to observe a similar EPR intensity within the two electrodes in
135 the pristine state. The observed contrast may have several physical origins such as, for example,
136 local variations of the microwave field caused by shielding or eddy current effects.⁹ After the
137 positive current flow (end of polarization 1, fig. 3b), the EPR intensity decreases in electrode Li_t
138 (top). Additional spots corresponding to metallic Li deposition appear on electrode Li_b (bottom),
139 and more particularly at the interface with the separator. The reverse phenomenon is observed
140 after inversion of the current flow (end of polarization 2, fig. 3c), with the metallic Li intensity
141 increasing on the surface of Li_t , near the separator, and an intensity decrease in Li_b . This imaging
142 mode, however, does not allow distinguishing clearly the two types of metallic Li.

143 In order to map the distribution of metallic lithium while preserving the spectroscopic (line-
144 shape, resonance field) information, we turned to the correlation of spectroscopy and imaging
145 (spectral-spatial EPR). This technique consists in scanning the whole cell with the field gradient

146 (175 G/cm) applied along the **Y** direction (cell axis). The image (electron density profile) is re-
147 constructed by stacking the EPR spectra obtained for each slice along the **Y** axis. In the resulting
148 two-dimensional plots shown in fig. 3 (right) the shape, resonance field and intensity of the EPR
149 spectra can be determined for each slice along the **Y** cell axis. For clarity the plot indicates the
150 variation of the absolute value of the first derivative signal $|d\chi''/dH|$ with the external magnetic
151 field. In this representation the spectra consist in two lobes along **H** separated by a narrow domain
152 with zero intensity. The main features of the EPR spectra can be recognized: (i) the field splitting
153 between the two lobes gives the peak-to-peak linewidth, ΔH of the EPR line, (ii) the relative inten-
154 sity of the two lobes gives the asymmetry ratio A/B , and (iii) the boundary between the two lobes
155 is the value H_{res} of the external field H_0 at which resonance occurs, as indicated by dashed lines
156 and white triangles.

157 The spatial distribution of the two types of lithium was obtained more precisely with these
158 spectral-spatial images. Initially, both electrodes show similar spectral characteristics, i.e. a broad
159 signal with the low field lobe more intense than the high field one, revealing the presence of only
160 bulk lithium foils (fig. 3d). Several modifications are observed at the end of polarization 1 (fig 3e):
161 (i) the EPR line is more intense in electrode Li_b than in electrode Li_t , and reveals the submicromet-
162 ric Li deposition on the bottom electrode, in agreement with spatial-spatial imaging. Interestingly
163 (ii) the intensity of the top (depleted) electrode is higher than in the pristine state. This effect is
164 the consequence of the roughening of the electrode surface upon stripping (increase of the volume
165 probed within the skin depth), in good agreement with our interpretation of pure EPR spectroscopy
166 (fig 2b). In addition, (iii) the linewidth of bulk Li decreases in both electrodes, in agreement with

167 fig. 2c. More importantly, in fig. 3e (iv) H_{res} of the top part of the Li_b electrode is slightly shifted
168 to lower field (white triangle) compared to the bottom part of the same electrode (vertical dashed
169 line). This result indicates that the sub-micrometric particles appear at the interface with the sep-
170 arator and not in the bulk of the bottom electrode. This trend is magnified, though in the opposite
171 direction, at the end of polarization 2 (current reversed) in fig. 3f: (i) the bottom electrode is sig-
172 nificantly depleted, while the signal of the top electrode is narrower, more intense and symmetrical
173 at the interface with the separator; (ii) H_{res} of the bottom part of electrode Li_t (white triangle)
174 is again shifted to lower field with respect to the top part (dashed line). These features indicate
175 the nucleation of an increased number of sub-micrometric Li particles at the electrode-separator
176 interface.

177 Finally, let us discuss the well-known problem of dendritic lithium nucleation which ulti-
178 mately leads to short-circuit. Fig. 4 focuses on an *in situ* dendrite-induced short-circuit in another
179 symmetric Li//Li cell. This phenomenon is visible in the galvanostatic profile in fig. 4a. We de-
180 tected a sudden drop to 0 V after almost 38 hours of cycling with the current still flowing, which
181 is indicative of a global short-circuit. The corresponding evolution of the EPR intensity and A/B
182 of the entire spectrum are given in fig. 4b. The intensity initially increases while A/B decreases.
183 This indicates a progressive increase in the number of electron spins submitted to the microwave
184 field, a signature of sub-micrometric Li particles nucleation and of the roughening of the elec-
185 trodes. After the short-circuit however, the intensity no longer varies with time, in agreement with
186 the failure of the cell. Fig. 4c shows the EPR spectra recorded (i) in the pristine state and (ii)
187 after the short-circuit. The broad and asymmetric lineshape of (i) corresponds to the bulk lithium

188 electrodes. The second spectrum (ii) appears at lower field, symmetrical and more intense than (i)
189 by a factor ~ 100 . This intense and very sharp peak associated with the short-circuit corresponds
190 to a large predominance of sub-micrometric Li particles, i.e. the modification of the morphology
191 of the whole lithium disks. It is important to note that Li dendrites with sub-micrometric thickness
192 may also contribute to this signal. This hypothesis is confirmed by the spatial-spatial EPR images
193 recorded in the pristine state (fig. 4d) and after the short-circuit (fig. 4e). The presence of a dendrite
194 is evidenced by a red spot on the right-hand side of fig. 4e that crossed the separator and short-
195 circuited the cell. Note that the top electrode was not consumed entirely; its intensity is lower as
196 explained above, but we can detect it (inset in fig. 4e). Additional red signals are dispersed under
197 the bottom electrode (indicated by white crosses) and correspond to Li sub-micrometric particles
198 deposited on the current collector after the short-circuit.

199 **Conclusion**

200 We performed *in situ* EPR measurements on symmetric Li/LiPF₆/Li cells in operating conditions.
201 We establish *operando* EPR spectroscopy and *in situ* EPR spectral-spatial imaging as two highly
202 complementary tools to follow the changing morphology of metallic lithium during stripping and
203 to identify, localize and distinguish dendrites and sub-micrometric lithium particle during plat-
204 ing. Two main features were observed from the evolution of the EPR spectra and spectral-spatial
205 EPR images of metallic Li in the electrochemical cell during polarization: (i) the nucleation of
206 sub-micrometric Li particles at the interface between the separator and the electrodes; (ii) the pro-
207 gressive roughening of the electrodes into fragments of size slightly larger than 1 μm . We also

208 provide an *in situ* EPR image of dendrites in the separator between the two electrodes, at the origin
209 of a short-circuit of the electrochemical cell. To the best of our knowledge, spectral-spatial EPR
210 imaging was never used to investigate such electrochemical devices and we hope that these results
211 will pave the way to the combination of *operando* EPR spectroscopy and *in situ* spectral-spatial
212 EPR imaging to diagnose new generations of lithium-ion batteries.

213 **Methods**

214 **Electrochemical cell** The symmetric Li/LiPF₆/Li electrochemical cells were assembled in the
215 homemade EPR cell previously developed⁶ using an argon-filled glove box. The current collectors
216 were copper disks on each side. The electrodes were metallic lithium disks with a typical thickness
217 of around 400 μm and a diameter of 5 mm. One piece of porous microfiber mat (Whatman type
218 GF/D) was used to separate the electrodes. The whole content of the EPR cell was soaked with
219 electrolyte (1 mol/L LiPF₆ in a mixture of ethylene and dimethyl carbonate in weight ratio 1:1,
220 Merck). Galvanostatic control was performed at room temperature using a VSP galvanostat from
221 Bio-Logic. The EPR cell was polarized (polarizations 1 and 2 in fig. 1a) with a current density
222 of 1 mA/cm². The current was paused at the end of polarization 1 to record the images. EPR
223 spectra were recorded continuously during polarization with a time resolution of 5 min (*operando*
224 EPR spectroscopy). The same procedure was used for polarization 2, with a current of -1 mA/cm².
225 The second EPR cell was polarized with a current density of 0.63 mA/cm² for 3 hours and -
226 0.63 mA/cm² for 3 hours. It was polarized positively again, with the same current as before,
227 during 20 hours to observe the nucleation of dendrites.

228 ***In situ* EPR** *In situ* continuous wave (cw) electron paramagnetic resonance experiments were
229 carried out using a conventional X-band Bruker E500 spectrometer operating at around 9.6 GHz
230 and room temperature. The microwave power supplied into the resonator was set to 4 mW in
231 order to avoid saturation of the EPR signal. The 100 kHz modulation depth of the magnetic field
232 was set to 0.1 mT or less to prevent distortion due to over-modulation. Conversion time and time
233 constant were set to 40.96 ms and 20.48 ms respectively. Cw-EPR spectra were fitted with one
234 dysonian and one derivative of Lorentzian using Matlab. The resonance fields of bulk (dysonian)
235 and sub-micrometric Li (Lorentzian) were fixed at 349.15 and 349.12 mT respectively.

236 The spectral-spatial and spatial-spatial images were recorded with a field-of-view of 7 mm
237 and gradient strength of 175 G/cm. The size of spatial-spatial images was 512×512 pixels re-
238 sulting in a pixel size of $13.7 \mu\text{m}$. The high resolution spatial-spatial EPR images were obtained
239 after a deconvolution of the acquired projections under a magnetic field gradient from a signal
240 recorded without gradient and a filtered back-projection. 140 projections were recorded for the
241 spectral-spatial images with a spectral resolution of 1024 points and a pixel size of $13.7 \mu\text{m}$ in
242 the spatial dimension. The high resolution spectral-spatial images were obtained from a filtered
243 back-projection of the acquired projections.

244 **Acknowledgements** This work was supported by the Agence Nationale de la Recherche (ANR) under a
245 JCJC project (ANR-15-CE05-0015-01) and LABEX STORE-EX (ANR-10-LABX-76), by the CNRS and
246 the RS2E (Réseau sur le Stockage Electrochimique de l'Energie) network. C-ED, ES and HV thank R.
247 Omnée and M. Deschamps for valuable discussions. C-ED, ES and HV thank CNRS's research federation
248 RENARD (FR3443) for EPR facilities.

249 **Author contributions** E.S., J.-M.T. and H.V. designed the project. C.-E.D., M.T. and H.V. performed the
250 EPR measurements, C.-E.D., E.S., D.G. and H.V. interpreted the results. The manuscript was drafted by
251 C.-E.D. and E.S. and revised by all authors.

252 **Competing Interests** The authors declare no competing interests.

253 **Correspondence** Correspondence and requests for materials should be addressed to C.-E.D.

254 (email: charles.dutoit@chimieparistech.psl.eu) and to H.V. (email: herve.vezin@univ-lille1.fr).

255 1. Liu, K., Liu, Y., Lin, D., Pei, A. & Cui, Y. Materials for lithium-ion battery safety. *Science*
257 *Advances* **4** (2018).

258 2. Waldmann, T., Hogg, B. I. & Wohlfahrt-Mehrens, M. Li plating as unwanted side reaction in
259 commercial Li-ion cells – A review. *Journal of Power Sources* **384**, 107–124 (2018).

260 3. Hatzell, K. B. *et al.* Challenges in lithium metal anodes for solid-state batteries. *ACS Energy*
261 *Letters* **5**, 922–934 (2020).

262 4. Liu, Q. *et al.* Understanding undesirable anode lithium plating issues in lithium-ion batteries.
263 *RSC Advances* **6**, 88683–88700 (2016).

264 5. Foroozan, T., Sharifi-Asl, S. & Shahbazian-Yassar, R. Mechanistic understanding of li den-
265 drites growth by in- situ/operando imaging techniques. *Journal of Power Sources* **461**, 228135
266 (2020).

267 6. Sathiya, M. *et al.* Electron paramagnetic resonance imaging for real-time monitoring of li-ion
268 batteries. *Nature Communications* **6** (2015).

- 269 7. Wandt, J. *et al.* Operando electron paramagnetic resonance spectroscopy – formation of mossy
270 lithium on lithium anodes during charge–discharge cycling. *Energy Environ. Sci.* **8**, 1358–
271 1367 (2015).
- 272 8. Wandt, J., Jakes, P., Granwehr, J., Eichel, R.-A. & Gasteiger, H. A. Quantitative and time-
273 resolved detection of lithium plating on graphite anodes in lithium ion batteries. *Materials*
274 *Today* **21**, 231 – 240 (2018).
- 275 9. Niemöller, A., Jakes, P., Eichel, R. A. & Granwehr, J. EPR Imaging of Metallic Lithium
276 and its Application to Dendrite Localisation in Battery Separators. *Scientific Reports* **8**, 1–7
277 (2018).
- 278 10. Dyson, F. J. Electron spin resonance absorption in metals. ii. theory of electron diffusion and
279 the skin effect. *Phys. Rev.* **98**, 349–359 (1955).
- 280 11. Feher, G. & Kip, A. F. Electron spin resonance absorption in metals. i. experimental. *Phys.*
281 *Rev.* **98**, 337–348 (1955).
- 282 12. Overhauser, A. W. Polarization of nuclei in metals. *Physical Review* **92**, 411–415 (1953).
- 283 13. Vigreux, C., Binet, L. & Gourier, D. Bistable Conduction Electron Spin Resonance in Metallic
284 Lithium Particles. *The Journal of Physical Chemistry B* **102**, 1176–1181 (1998).
- 285 14. Vigreux, C., Loiseau, P., Binet, L. & Gourier, D. Anomalous metallic lithium phases: Identifi-
286 cation by ESR, ENDOR, and the bistable Overhauser effect. *Physical Review B - Condensed*
287 *Matter and Materials Physics* **61**, 8759–8770 (2000).

- 288 15. Hope, M. A. *et al.* Selective NMR observation of the SEI-metal interface by dynamic nuclear
289 polarisation from lithium metal. *Nature communications* **11**, 2224 (2020).
- 290 16. Maresch, G. G., Mehring, M. & Emdin, S. High resolution ESR imaging. *Physica B+C* **138**,
291 261–263 (1986).